ADVANCED MATERIALS
www.advmat.de

Kinetically Controlled Synthesis of Metallic Glass Nanoparticles with Expanded Composition Space

Bing Deng, Zhe Wang, Chi Hun Choi, Gang Li, Zhe Yuan, Jinhang Chen, Duy Xuan Luong, Lucas Eddy, Bongki Shin, Alexander Lathem, Weiyin Chen, Yi Cheng, Shichen Xu, Qiming Liu, Yimo Han, Boris I. Yakobson, Yufeng Zhao,* and James M. Tour**

Nanoscale metallic glasses offer opportunities for investigating fundamental properties of amorphous solids and technological applications in biomedicine, microengineering, and catalysis. However, their top-down fabrication is limited by bulk counterpart availability, and bottom-up synthesis remains underexplored due to strict formation conditions. Here, a kinetically controlled flash carbothermic reaction is developed, featuring ultrafast heating (>10^5 K s^{-1}) and cooling rates (>10^4 K s^{-1}), for synthesizing metallic glass nanoparticles within milliseconds. Nine compositional permutations of noble metals, base metals, and metalloid (M_1—M_2—P, M_1 = Pt/Pd, M_2 = Cu/Ni/Fe/Co/Sn) are synthesized with widely tunable particle sizes and substrates. Through combinatorial development, a substantially expanded composition space for nanoscale metallic glass is discovered compared to bulk counterpart, revealing that the nanosize effect enhances glass forming ability. Leveraging this, several nanoscale metallic glasses are synthesized with composition that have never, to the knowledge, been synthesized in bulk. The metallic glass nanoparticles exhibit high activity in heterogeneous catalysis, outperforming crystalline metal alloy nanoparticles.

1. Introduction

Metallic glasses (MGs) are a broad class of solid metallic materials with amorphous atomic structures.[1] Depending on the glass forming ability (GFA) that quantitatively described by critical cooling rate (R_C), MGs exhibit many dimensional forms. For example, MG ribbons, typically <100 µm, are made by rapid quenching of alloy melts,[2] MG thin films are fabricated by physical vapor deposition,[3] and bulk MGs with low R_C are afforded by casting.[4] Recently, MG nanostructures have received considerable interests due to their unique atomic structures,[5] intriguing size-dependent mechanics,[6] and the potential application in unconventional areas including additive manufacturing,[7] nanoimprinting,[8] and catalysis.[9] The present top-down fabrication of MG nanostructures involves thermoplastic forming,[8,9d,10] thermal drawing techniques,[11] selective etching,[12] and laser ablation.[13] However, the top-down approaches rely on bulk MG counterpart availability, which restricts the material and composition choice. The bottom-up nanoscale MG synthesis such as chemical reduction,[6a,14] electrochemical synthesis,[9a,15] and physical vapor deposition,[16] affords better size, morphology, and compositional tunability. However, wet-chemistry-based processes often lead to contamination by surfactants,[14c] while

---

B. Deng, Z. Wang, G. Li, Z. Yuan, J. Chen, D. X. Luong, L. Eddy,
A. Lathem, W. Chen, Y. Cheng, S. Xu, Q. Liu, B. I. Yakobson, J. M. Tour
Department of Chemistry
Rice University
Houston, TX 77005, USA
E-mail: dengbing@tsinghua.edu.cn; tour@rice.edu

B. Deng
School of Environment
Tsinghua University
Beijing 100084, China

C. H. Choi, B. Shin, Y. Han, B. I. Yakobson, J. M. Tour
Department of Materials Science and NanoEngineering
Rice University
Houston, TX 77005, USA

D. X. Luong, L. Eddy, A. Lathem
Applied Physics Program
Rice University
Houston, TX 77005, USA

B. I. Yakobson, J. M. Tour
Smalley-Curl Institute
Rice University
Houston, TX 77005, USA

Y. Zhao
Department of Science and Mathematics
Corban University
5000 Deer Park Drive SE, Salem, OR 97317, USA
E-mail: yzhao@corban.edu

J. M. Tour
NanoCarbon Center and the Rice Advanced Materials Institute
Rice University
Houston, TX 77005, USA

The ORCID identification number(s) for the author(s) of this article can be found under https://doi.org/10.1002/adma.202309956

DOI: 10.1002/adma.202309956

physical deposition methods require a substrate that hinders intrinsic property studies and wide-range applications.

It is highly desired but still challenging to develop a bottom-up method for synthesizing nanoscale MG with tunable compositions, small size, and good morphology. A thermal process for nanoscale MG synthesis necessitates certain features. First, a high temperature is necessary to ensure the intimate mixing of multiple metal elements with diverse miscibility, as MGs are typically composed of three or more elements.[1] Second, a short reaction duration is required to minimize particle agglomeration and achieve uniform, nanoscale particle dispersion. Finally, an ultrafast cooling rate is needed to vitrify the alloy melt and avoid crystallization. Recently, several unconventional thermal processes[17] have been reported for synthesizing alloy nanoparticles with single-phase crystal structures, such as the electrothermal-based shock synthesis of high-entropy alloy nanoparticles,[18] the photothermal-based laser ablation synthesis of high-entropy alloy and ceramic nanoparticles,[19] and the flash Joule heating synthesis of metastable nanocrystals.[20] We anticipate that by rational composition design, nonequilibrium thermal processes can kinetically suppress crystallization and produce metastable glassy materials.

In this context, we here report the flash carbothermic reaction (FCR) for the general synthesis of metallic glass nanoparticles (MGNPs). Metal precursors loaded on a carbon substrate are subjected to millisecond current pulses, rapidly raising the temperature to ≈1800 K through Joule heating ($>10^5$ K s^{-1}). The resulting alloy melts then cool at an ultrafast rate ($>10^4$ K s^{-1}) through thermal radiation, vitrifying into glassy nanoparticles. FCR is feasible for the synthesis of various Pd- and Pt-based MGNPs, including palladium–nickel–phosphorous (PdNiP), PdCuP, PdCuNiP, PtCuP, PtCuNiP, and the high-entropy PtPdCuNiP. By constructing phase diagram of PdNiP nanoparticles through combinational development, we discover that the composition space of MG at the nanoscale is substantially expanded than that of the bulk counterpart, implying that the nanosize effect enhances the GFA. Structural simulations further reveal delicate short-range order differences between nanoscale and bulk MG. Importantly, the enhanced GFA allows for the synthesis of nanoscale MG with compositions that have never been achieved in bulk, exemplified by PdCoP, PdSnP, and high-entropy PdCuFeNiP. Furthermore, we demonstrated applications of MGNP in heterogenous catalysis, outperforming the crystalline counterparts.

2. Results

2.1. Synthesis of PdNiP MGNP by Flash Carbothermic Reaction

FCR for MGNP synthesis involves three steps (**Figure** 1a). First, metal precursors were dissolved in ethanol and homogeneously impregnated onto a carbon black support, which served as both a conductive additive and a supporting substrate (Figures S1 and S2, Supporting Information). Second, pulsed direct current input rapidly raised the sample temperature,[18a,21] leading to the decomposition of metal salt precursors into elemental liquid metals (equations in Figure 1a). Since these metals do not wet carbon, the liquid metals diffuse to reduce their surface energy at high temperature, and subsequently fuse into alloy melts driven by the negative enthalpy of mixing (ΔH_{mix}).[22] Finally, the sample rapidly cooled due to the intensive thermal radiation and low heat capacity of carbon substrate (<0.033 J K^{-1}),[23] resulting in the vitrification of alloy melt into glassy nanoparticles (Figure 1b). Due to the good GFA of ternary PdNiP, it is chosen for the initial trials.[4b] A pulsed current of ≈90 A within 50 ms was applied to the precursor mixture in an Ar-filled chamber (Figure 1c and Figure S3 (Supporting Information)). With strong light emission (Figure 1c, inset), the sample temperature rapidly reached its maximum at T_{max} ≈1760 K (Figure 1d), beyond the decomposition temperature of metal precursors (Table S1, Supporting Information). Based on T_{max} and the glass transition temperature (T_g) of PdNiP (≈600 K),[24] the cooling rate was calculated to be $\approx 1.5 \times 10^4$ K s^{-1}, higher than the R_C of PdNiP bulk MG.[25]

Deviating from thermodynamically equilibrium crystal phases, metallic glass is typically trapped by a kinetic barrier. According to the temperature–time transformation diagram, as schematically shown in Figure 1e, the cooling rate determines the formation of glassy or crystal phases. In the scenario of FCR, the rapid cooling enables the glassy phase formation. As a control, the synthesis using a tube furnace with a slow cooling rate (≈10 K min^{-1}) led to the formation of crystalline PdNiP nanoparticles (Figure S4, Supporting Information).

2.2. Characterization of PdNiP MGNP

The amorphous structure of the PdNiP nanoparticles was confirmed by X-ray diffraction (XRD) and transmission electron microscopy (TEM). The XRD pattern did not show any peaks from crystalline components, except for the broad diffraction peaks from the amorphous carbon support (**Figure** 2a). The synthesized nanoparticles are supported on carbon black (Figure 2b). The selected-area electron diffraction (SAED) shows diffusive diffraction halos without discrete spots (Figure 2b, inset). The amorphous structure was further confirmed by high-resolution TEM (HRTEM) and the corresponding fast Fourier transformation (FFT) pattern (Figure 2c). HRTEM images with tilt angle from 0° to 5° were acquired and all are characterized of an amorphous structure (Figure S5, Supporting Information). To exclude the effect of the carbon support, nanobeam diffraction was performed on a single nanoparticle, which showed similar diffuse halos (Figure 2d, inset). The normalized intensity of the nanobeam diffraction pattern showed the main peak positions at 4.12 and 6.96 nm^{-1}, corresponding to k_2/k_1 ≈1.69 (Figure 2d), in agreement with previous experimental results on PdNiP bulk MG.[26] The particle size was calculated based on the data from the TEM images, showing an average size of ≈10.6 nm and a narrow size distribution (Figure 2e). The average composition was determined to be $Pd_{43}Ni_{26}P_{31}$ by energy-dispersive X-ray spectroscopy (EDS) (Text S1 (Supporting Information) and Figure 1f). Due to the short duration of the FCR process and the temperatures being ≤2500 K, the carbon substrates remain unchanged (Figure S6, Supporting Information). The high temperature of the FCR process results in the complete reaction, leaving no chloride residue in the product (Figure S7, Supporting Information).

We investigated the electronic structures of the PdNiP MGNP by X-ray photoemission spectroscopy (XPS) (Text S2 and Table S3 (Supporting Information) and Figure 2g–i). Various chemical bonds, including Pd—Pd, Ni—Ni, P—P, Pd—Ni, Pd—P, and

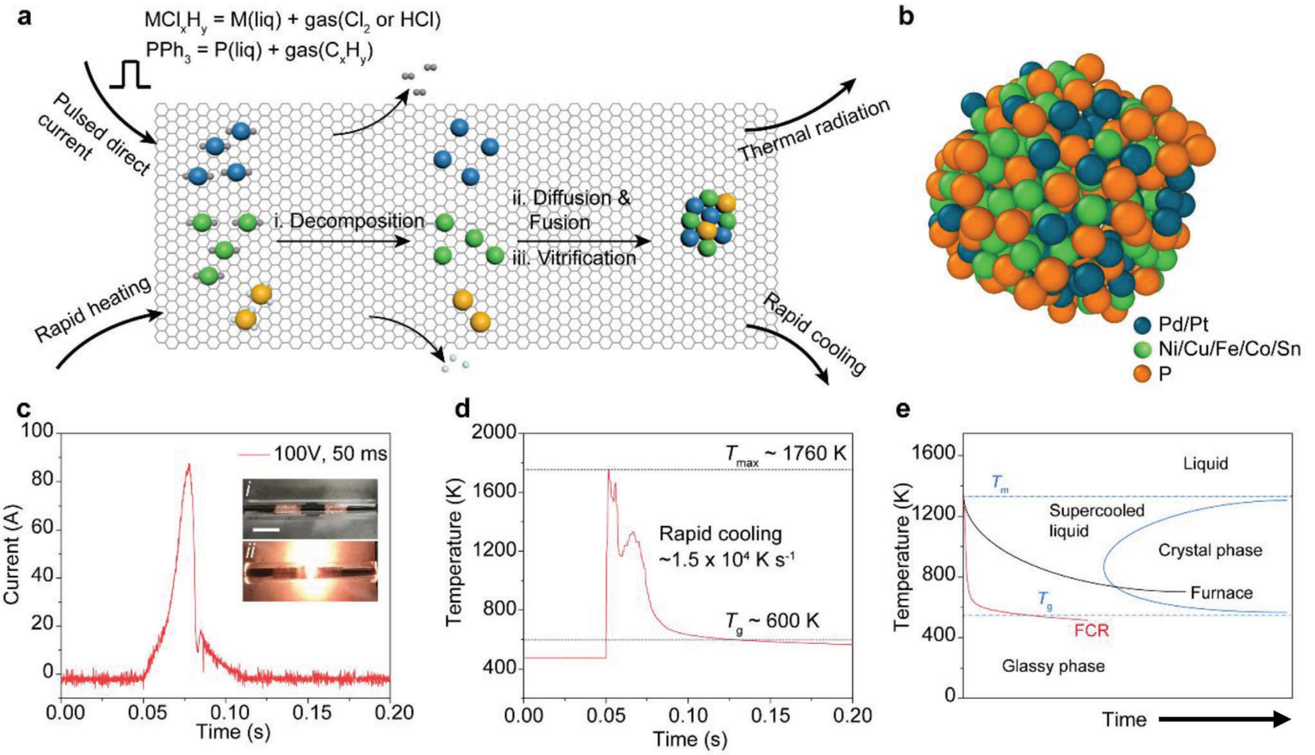

Figure 1. Synthesis of MGNP by flash carbothermic reaction. a) Schematic of the FCR process for MGNP synthesis. b) Molecular dynamics simulated atomic model of a ternary MGNP. c) Pulsed current curve under the FCR conditions of 100 V and 50 ms. Inset, the pictures of the sample before (top) and during (bottom) the FCR reaction. Scale bar, 1 cm. d) Real-time temperature curve recording using an infrared thermometer. T_{max} and T_g are the maximum temperature of the FCR process and the glass transition temperature of PdNiP, respectively. e) Schematic of the time–temperature transformation diagram showing the kinetic formation of MG. T_m and T_g are the melting temperature and the glass transition temperature of PdNiP, respectively.

Ni—P, were found, resulting from its amorphous feature. The Pd 3d is split into two peaks of Pd $3d_{5/2}$ and $3d_{3/2}$ (Figure 2g). The Pd $3d_{5/2}$ peak at 335.4 eV is assigned to Pd—M (including Pd—Pd[27] and Pd—Ni[28]). The Pd $3d_{5/2}$ peak at 337.0 eV is assigned to Pd—P.[29] The minor Pd $3d_{5/2}$ peak at 338.3 eV could be assigned to be Pd—O[30] due to the surface oxidation. The Ni $2p_{3/2}$ peak at 852.9 eV is assigned to Ni—P, and the peak at 857.0 eV is its satellite peak[31] (Figure 2h). The minor Ni $2p_{3/2}$ peak at 854.3 eV can be assigned to Ni—O due to surface oxidation. The P 2p is split into two peaks of P $2p_{3/2}$ and $2p_{1/2}$. For P $2p_{3/2}$, the peak at 130.5 eV is assigned to P—M,[32] and the peak at 132.5 eV could be assigned to M—P—O due to surface oxidation (Figure 2i).

2.3. General Synthesis of Pd- and Pt-Based Metallic Glass Nanoparticles

To demonstrate the versatility of our FCR method, a series of Pd- and Pt-based MGNPs were synthesized (**Figure 3** and Tables S2 and S3 (Supporting Information)). Typically, the GFA of an alloy is susceptible to its composition, where even the difference of a few atomic ratio percentages could induce a change of R_C by several orders of magnitude.[33] Nevertheless, due to the presence of deep eutectics in the Pd—P and Pt—P systems, Pd- and Pt-based MG can be synthesized over a wide compositional range.[34] To control product composition, we employed an excessive supply of P, given its higher volatility compared to other metal components (Tables S1 and S2, Supporting Information). The amorphous features of the synthesized nanoparticles were confirmed through multiscale characterization methods, including XRD, SAED, and HRTEM. The average compositions were $Pd_{43}Ni_{26}P_{31}$ (Figure 3a), $Pd_{48}Cu_{30}P_{22}$ (Figure 3b and Figures S8–S10 (Supporting Information)), $Pt_{34}Cu_{38}P_{28}$ (Figure 3c and Figures S11–S13, Supporting Information), $Pd_{49}Cu_{13}Ni_8P_{30}$ (Figure 3d and Figures S14–S16 (Supporting Information)), $Pt_{48}Cu_{14}Ni_{11}P_{27}$ (Figure 3e and Figures S17–S19 (Supporting Information)), and the quinary $Pt_{21}Pd_{32}Cu_{11}Ni_9P_{27}$ (Figure 3f and Figures S20–S22 (Supporting Information)), which is considered a high-entropy MG.[9a,35] High-angle annular dark-field scanning transmission electron microscopy (HAADF-STEM) image and element maps demonstrated uniform distributions of elements. The nanoparticles exhibited structural and elemental uniformity, regardless of their compositions. The EDS spectra of individual nanoparticles of all compositions show the absence of carbon or oxygen peaks (Figure 3a for PdNiP, Figure 3b for PdCuP, Figure 3c for PtCuP, etc.), proving that the as-synthesized nanoparticle is metallic glass, instead of oxide glass or carbide phase. The carbon black serves as the conductive additive and substrate and does not participate in the reaction.

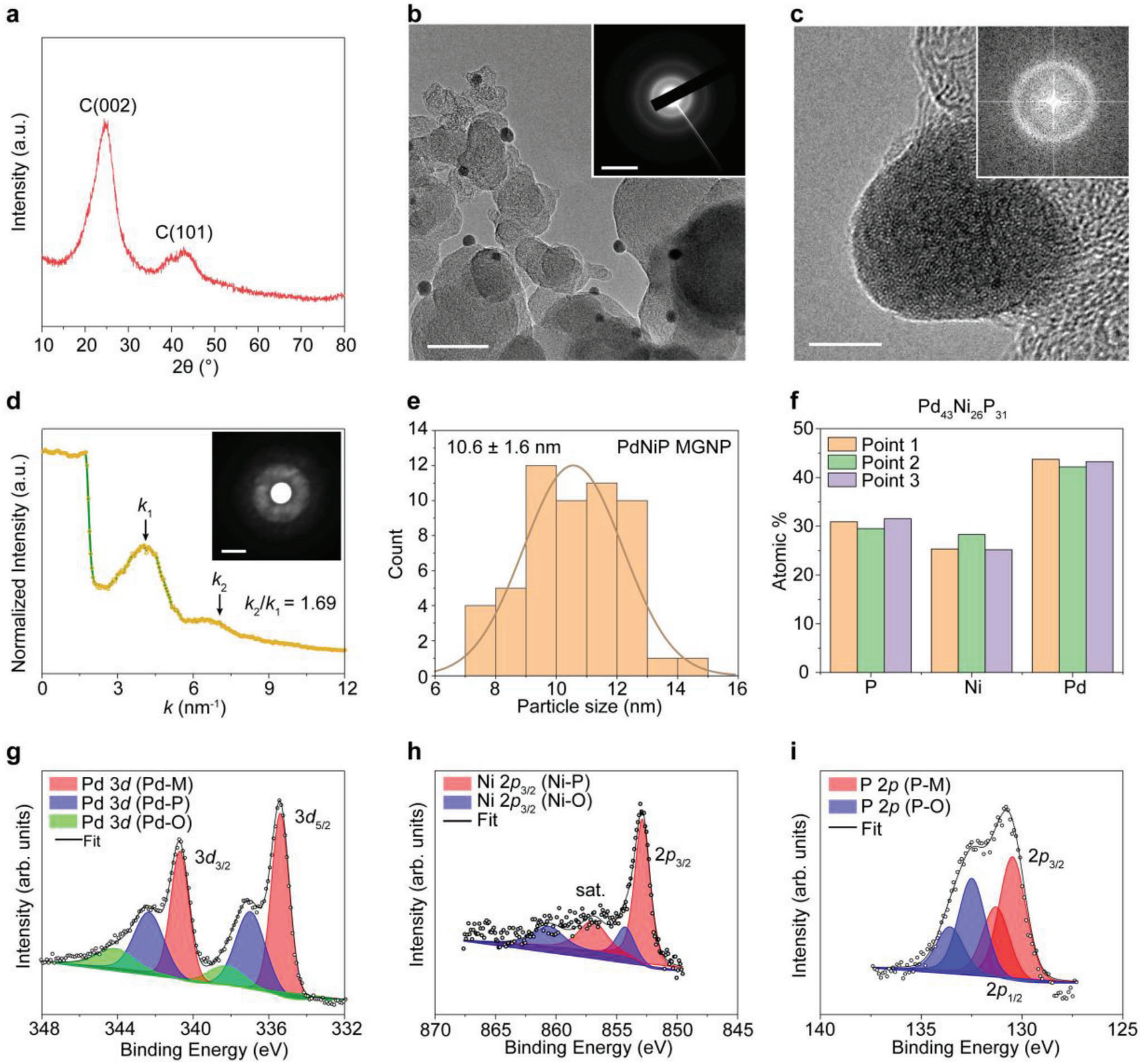

Figure 2. Characterization of the PdNiP MGNP. a) XRD pattern of the PdNiP MGNP supported on carbon black. The PDF reference card is graphite (PDF#41-1487). b) Bright-field transmission electron microscopy (BF-TEM) image of the PdNiP MGNP supported on carbon black. Inset, SAED pattern of the MGNP supported on carbon black. The scale bar is 50 nm for the TEM image, and 5 nm^{-1} for the SAED pattern. c) HRTEM image of the PdNiP MGNP and the corresponding FFT image (inset). Scale bar, 5 nm. d) Nanobeam diffraction pattern of the PdNiP MGNP, and the intensity profile derived from the electron diffraction. k_1 and k_2 are the first and second diffraction vectors, respectively. Scale bar, 5 nm^{-1}. e) Size distribution of the PdNiP MGNP. The average size is 10.6 ± 1.6 nm. f) Elemental composition of the PdNiP MGNP determined by EDS. Three points were collected with the average composition of Pd$_{43}$Ni$_{26}$P$_{31}$. g) XPS fine spectrum of Pd. h) XPS fine spectrum of Ni. i) XPS fine spectrum of P.

The FCR method for MGNP synthesis offers wide tunability in terms of particle size, dispersity, composition, and substrate. The MGNPs show a narrow size distribution with variation <10%. The particle size can be tuned by varying precursor loadings (Figure S23, Supporting Information) or the FCR time durations (Figure S24, Supporting Information), but particle size cannot be adjusted independently from loading. The synthesized MGNPs were uniformly dispersed on the carbon black support, and other conductive carbons like carbon nanotubes can also be used (Figure S25, Supporting Information), expanding the range of substrate applicability. However, our FCR process is currently not compatible with insulative substrates like TiO$_2$, Al$_2$O$_3$, etc. Importantly, the MGNPs remained stable in atmospheric conditions and preserve their structure, size, and morphology even after 6 months of storage (Figure S26, Supporting Information). The FCR process for MGNP

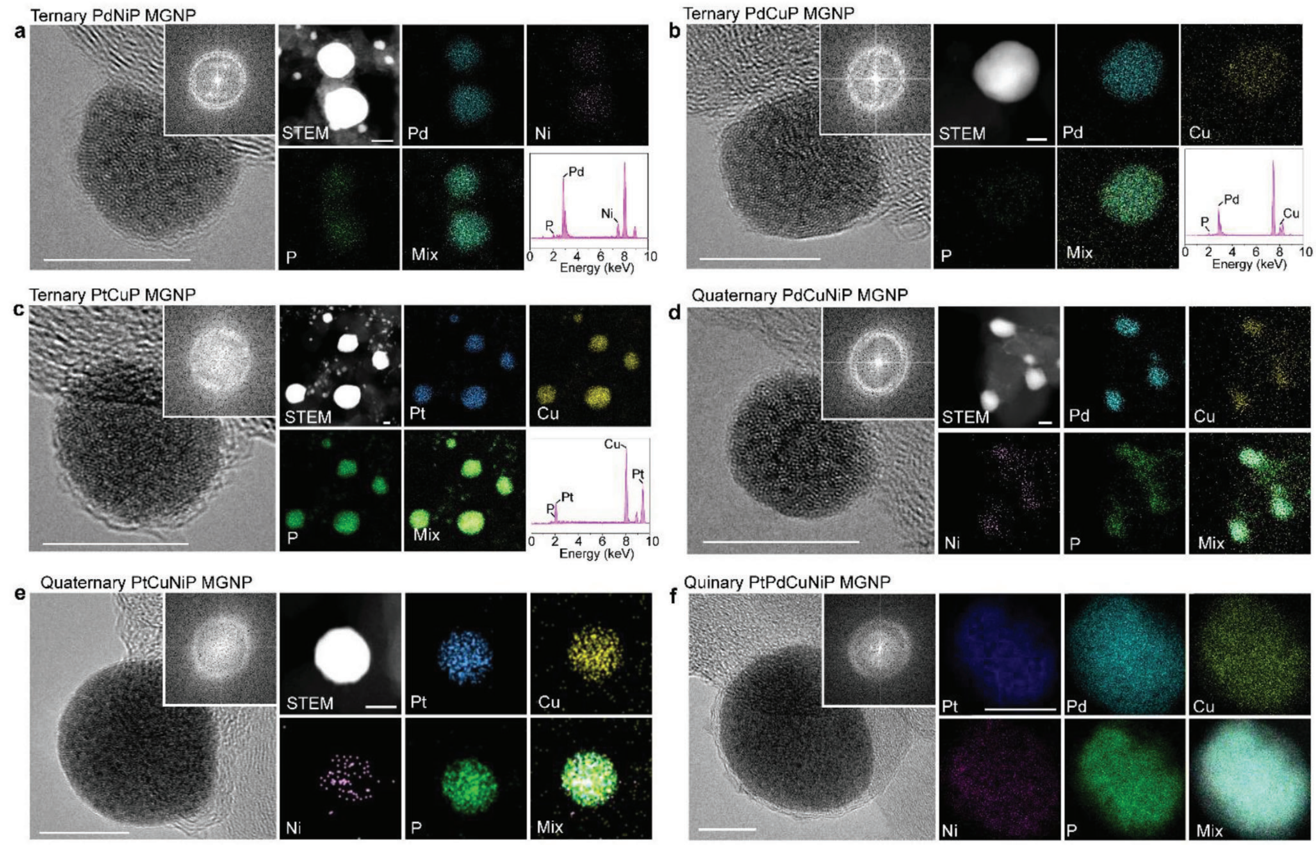

Figure 3. General synthesis of MGNP by the FCR process. HRTEM images, the corresponding FFT patterns, HAADF-STEM images, elemental maps, and EDS spectra for a) ternary PdNiP MGNP, b) ternary PdCuP MGNP, c) ternary PtCuP MGNP, d) quaternary PdCuNiP MGNP, e) quaternary PtCuNiP MGNP, and f) quinary, high-entropy PtPdCuNiP MGNP. All scale bars in the HRTEM images and STEM images are 10 nm.

synthesis is also scalable. By simply increasing the FCR voltage, we achieved a batch size of 0.2 g (Text S3 and Figure S27, Supporting Information). Considering the time used to charge the FCR system and the loading of the sample, we conclude that the time required for the 200 mg batch synthesis is ≈10 s, corresponding to a production rate of 72 g h^{-1}, higher than other reported methods like chemical reduction, electrochemical synthesis, and physical vapor deposition (Figure S28, Supporting Information).

2.4. Nanosize Effect Enhanced Glass Forming Ability

Combining easily tunable precursor loading and ultrafast synthesis, the FCR provides access to a broad compositional space of MG. By combinatorial development, we synthesized a large library of ternary PdNiP nanoparticles, whose phases (crystalline or glassy) and compositions were determined by TEM and EDS, respectively (**Figure** 4a). The Pd—Ni—P phase diagram revealed that ≈54% of the nanoparticles formed a glassy phase, covering about 10–55 at% of P. In comparison, the compositions of ribbon MG[36] and bulk MG[25] appear to lie close to P ≈20 at% (Figure 4a), which is rooted in the deep eutectic points at approximately $Ni_{80}P_{20}$ and $Pd_{80}P_{20}$. Therefore, the composition space of PdNiP MG at the nanoscale is substantially larger than its bulk counterpart, i.e., the nanosize effect enhances the glass forming ability.

The R_C determines whether the phase is crystalline or glassy under a specific cooling rate. The composition-dependent R_C was calculated for the Pd—Ni—P system using an empirical model[37] and a recently developed algorithm[38] (Figure 4b; computational details in Text S4 in the Supporting Information). The R_C strongly correlates with the P content, with compositions of 20–70 at% of P having R_C <100 K s^{-1} (Figure 4b). For P content <10 or >80 at%, the R_C surges to >10^4 K s^{-1}. As the cooling rate of our FCR is on the order of 10^4 K s^{-1} (Figure 1d), it affords the synthesis of PdNiP MGNP with P content as low as ≈10 at% (Figure 4b). This is consistent with experimental results, where crystalline phases form at P <10 at% (Figure 4a).

To further explain the size-dependent GFA, ab initio molecular dynamics was implemented to explore the MG structure in both the nanoparticulate and bulk forms. We modeled a PdNiP nanoparticle surrounded by a vacuum layer (Figure 4c) and a PdNiP supercell under periodic boundary conditions (Figure 4d), both having the same composition ratio (Pd:Ni:P ≈ 2:2:1). While both ensembles had amorphous atomic structures, the local bond orientational order was employed to quantitatively describe the degree of disorder.[5,39] 100% atoms in the MG nanoparticle are disordered under the normalized bond orientational order parameter criterion (Figure 4e). By contrast, while most atoms

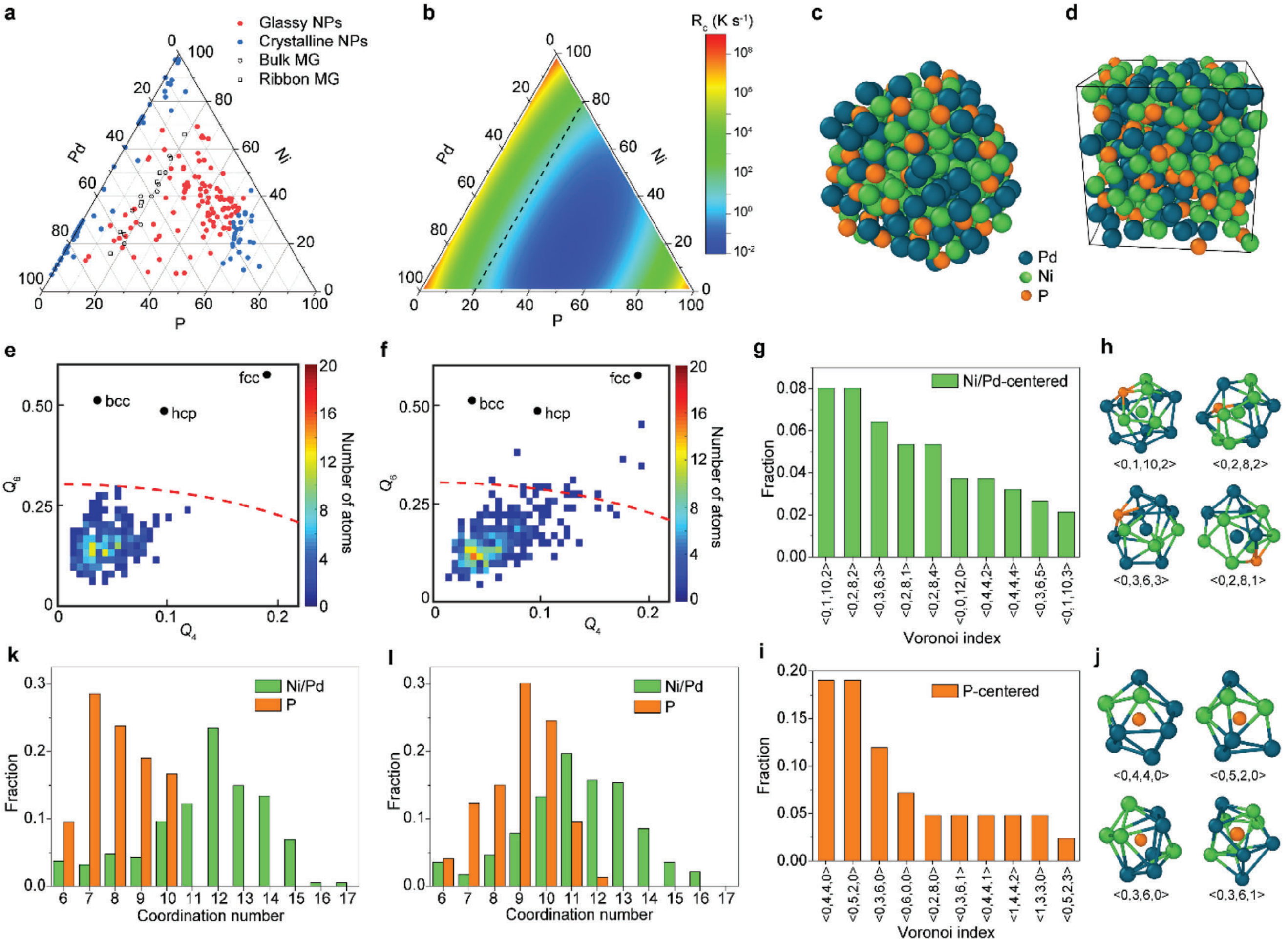

Figure 4. Nanoscale effect enhanced glass forming ability. a) The phase diagram of the ternary Pd—Ni—P system. The compositions of bulk MG and ribbon MG were from literatures values.[25,36] b) Calculated R_C of the ternary Pd—Ni—P system. The dashed line denotes the composition of P = 20 at%. c) Molecular dynamics simulated 3D atomic model of MG nanoparticle with composition of $Pd_{126}Ni_{127}P_{60}$ (P at% ≈19%). d) Molecular dynamics simulated 3D atomic model of MG bulk with composition of $Pd_{170}Ni_{170}P_{80}$ (P at% ≈19%). e,f) Local bond orientational order parameters of all the atoms in the MG nanoparticle (e) and the MG bulk (f). The dashed red curves denote the normalized bond orientational order parameter at 0.5, which serves as the criterion differentiating disordered and ordered structures. g) Ten most abundant Ni/Pd-centered Voronoi polyhedra in the MG nanoparticle. h) Four representative Ni/Pd-centered Voronoi polyhedra. i) Ten most abundant P-centered Voronoi polyhedra in the MG nanoparticle. j) Four representative P-centered Voronoi polyhedra. k) The coordination number distribution of Ni/Pd and P for MG nanoparticle. The average coordination numbers of Ni/Pd and P are 11.5 and 7.9, respectively. l) The coordination number distribution of Ni/Pd and P for MG bulk. The average coordination number of Ni/Pd and P are 11.1 and 8.8, respectively.

(≈96.4%) in the MG bulk are disordered, some have crystal features approaching hexagonal close packed (hcp) or face cubic center (fcc) structures (Figure 4f). These results demonstrate that, even with the same composition, the MG nanoparticle is more disordered than its bulk counterpart, echoing the experimental result that the nanosize effect enhances GFA. A series of MG with P content of −11, −19, −33, −40, and −52 at% were modeled (Figure *S29*, Supporting Information), where all nanoparticles are more disordered than the bulk counterparts, regardless of the composition (Figure S30, Supporting Information).

Furthermore, the subtle differences in short-range order between nanoscale and bulk MG were analyzed based on Voronoi tessellation.[5,40] In metal–metalloid MG, the metals (Ni, Pd) and metalloid (P) exhibit distinct local orders.[40b] The ten most prevalent Ni/Pd-centered Voronoi polyhedra in MG nanoparticle are depicted in Figure 4g. Common motifs observed in MG, such as distorted icosahedra with indices of <0, 1, 10, 2>, <0, 2, 8, 2>, <0, 2, 8, 1>, and <0, 3, 6, 3> are identified (Figure 4h). For the P-centered cases (Figure 4i), frequently encountered polyhedra include tricapped trigonal prisms with an index of <0, 3, 6, 0>, and distorted tricapped trigonal prisms with indices of <0, 4, 4, 0>, <0, 5, 2, 0>, and <0, 3, 6, 1> (Figure 4j). The Voronoi polyhedra of the MG bulk are mostly the same as those in the nanoparticle (Figure S31, Supporting Information). The polyhedral face distribution of all the Voronoi polyhedra shows the most prevalent 5-edged Ni/Pd-centered faces in both MG nanoparticle and bulk. By contrast, the 4-edged P-centered polyhedral faces are the most abundant in MG nanoparticle, and 5-edged ones in MG bulk (Figure S32, Supporting Information). Moreover, the coordination numbers of all the atoms in the MG were determined based on the Voronoi index from $\sum_i n_i$ (Figure 4k,l). The average first-neighbor coordination numbers of Ni/Pd in MG nanoparticle (≈11.5) are very similar to those in MG bulk (≈11.1). However, the average coordination numbers of P in MG nanoparticle (7.9) are smaller than MG bulk (8.8), clearly revealing the more disordered local structure of MG in nanoparticle form.

2.5. Synthesis of MGNP with Expanded Composition Space

The conclusion of the enhanced GFA in nanoscale MG has two implications. First, for a given alloy system, a composition ratio that cannot form bulk MG may form glassy material at the nanoscale. The strict composition requirement for bulk MG would be lessened for bottom-up nanoscale MG synthesis, as demonstrated by the synthesis of Pd—Ni—P MGNP with wide tunable composition (Figure 4a).

Second, an alloy system that is inaccessible for bulk MG may form MG at the nanoscale. Based on this, we further expanded the composition space of Pd-based MG. Combined with the composition-dependent R_C calculation as described earlier (Text S4, Supporting Information), the MGNP synthesis could be rationally designed. As examples, we here expanded the choice of base metals and achieved the synthesis of PdCoP (**Figure 5a–c** and Figure S33 (Supporting Information)) and PdSnP MGNPs (Figure 5d–f and Figure S34 (Supporting Information)). Due to the similar property of Co and Ni, the composition-dependent R_C for Pd—Co—P system (Figure 5a) resembles to that of Pd—Ni—P (Figure 4b), where P content is critical. By contrast, the calculated R_C of Pd—Sn—P (Figure 5d) shows that all three elements are critical for the glassy formation. Furthermore, we incorporated Fe and synthesized the high-entropy PdCuNiFeP MGNP (Figure 5g,h and Figures S35 and S36 (Supporting Information)). These MGNP compositions, to the best of our knowledge, have not yet been reported in bulk form, so we do not know whether they can be synthesized in bulk. This will inspire researchers to explore a wide range of glassy materials and high entropy materials[41] beyond current reports.

Due to the versatility of our developed FCR method, the synthesized MGNP can find wide applications in various fields. As a demonstration, we here showed the application of MGNP in heterogeneous catalysis (Text S5, Supporting Information), exemplified by Suzuki–Miyaura coupling of a boronic acid and an aryl halide (Table S4, Supporting Information). High yields (>99%) for different coupled biaryl products were obtained with the PdNiP MGNP catalyst under mild reaction conditions. The yields are higher than those of the bimetallic PdNi catalyst nanoparticles.[42] To assess the intrinsic catalytic performance of these Pd-based catalysts, the turnover frequency (TOF) was calculated. The TOF of the PdNiP MGNP is significantly higher than the bimetallic $Ni_{0.9}Pd_{0.1}$ and Pd_1Ni_4, demonstrating the high intrinsic activity of the PdNiP MGNP. This could be due to the optimized electronic structure by the synergic Pd—Ni—P interactions, as well as the geometric effect through which the amorphous structure has more active sites for catalysis. In addition, the Pd—Ni—P MGNP also exhibits high yields for catalytic coupling of aryl halides and styrene by Miyaura–Heck coupling (Text S5 and Table S5, Supporting Information).

3. Conclusion

In summary, we developed a kinetically controlled FCR process featuring ultrafast heating and cooling for the general synthesis of Pd- and Pt-based MGNPs with good control over their composition, particle size, dispersity, and supporting substrates. We discovered that the nanoscale MG has an expanded composition space than its bulk counterpart, indicating that the nanosize effect enhanced GFA, which could inspire exploration of the compositional space of nanoscale MG beyond the bulk form. The MGNPs show promising performance in heterogeneous catalysis. We anticipate that this method can be extended to synthesize a wide range of amorphous and metastable materials, thereby expanding the current crystal-phase-diagram-dominated material discovery.

4. Experimental Section

Materials: Metal salts, including H_2PtCl_6 (≥37.5 wt% Pt basis, Millipore-Sigma), $PdCl_2$ (99 wt%, Aldrich Chem), $CuCl_2$ (97 wt%, Sigma-Aldrich), $NiCl_2$ (98 wt%, Sigma-Aldrich), $FeCl_3$ (Fisher Scientific), $CoCl_2\cdot 6H_2O$ (Acros Organics), and $SnCl_4\cdot 2H_2O$ (98 wt%, Sigma-Aldrich), were used as metal precursors. Triphenylphosphine (PPh_3, 99 wt%, Acros Organics) was used as the phosphorus precursor. Carbon black (Carbot, Vulcan XC72) or carbon nanotubes (CNTs, MEIJO DIPS, single-walled CNT) was used as conductive additives and supports.

Precursor Loading: The metal precursors were dissolved in ethanol separately at a concentration of 0.05 м (Figure S1a, Supporting Information). $PdCl_2$ was dissolved in ethanol with 1 м HCl. The loading of Pd or Pt was fixed to 5 wt% with respect to carbon black. Then, the amount of other precursors, including Cu, Ni, Fe, Co, Sn, and P, was calculated according to a fixed molar ratio. For example, in the synthesis of ternary PdNiP MGNP, the molar ratio of Pd:Ni:P = 1:1:2 was used. Accordingly, the mass or volume for each precursor was carbon black (50 mg), $PdCl_2$ (0.05 м, 0.94 mL), $NiCl_2$ (0.05 м, 0.94 mL), and PPh_3 (0.05 м, 1.88 mL). The metal precursor solutions ($PdCl_2$ and $NiCl_2$) were mixed first, and then carbon black was added into the mixed solution. The slurry of carbon black and precursor solution was bath-sonicated (Cole-Parmer Ultrasonic Cleaner) for 10 min to enhance the dispersion, and then dried in a vacuum desiccator overnight (Figure S1b, Supporting Information). Next, the black power was added to the PPh_3 solution, followed by sonication, and drying in a vacuum desiccator overnight. It was crucial to follow the above sequence, i.e., first loading metal precursors and then P precursor, to prevent the reaction of Pd^{2+} with PPh_3 and form a complex that precipitated in the ethanol. The same protocol also prevented the formation of $PtCl_4{}^{2-}$ and PPh_3 complexes. The detailed precursor loading conditions for the synthesis of each MGNP, as well as the controlled samples, are listed in Table S2 (Supporting Information).

FCR System and Synthesis Process: The electrical diagram of the FCR system is presented in Figure S3a (Supporting Information). A mixture of carbon black and metal precursors was loaded into a quartz tube with an inner diameter of 4 mm. Graphite rods were used as the electrodes on both sides of the quartz tube. The quartz tube was set in a reaction jig and connected to the FCR system. The resistance of the sample was controlled by compressing the two electrodes. The reaction jig was placed inside a desiccator filled with Ar gas to prevent sample oxidation. The capacitor bank with total capacitance of 60 mF was charged by a DC supply capable of reaching 400 V. The discharging time was controlled by a relay with programmable delay time, accurate to millisecond. The specific parameters for synthesizing the various MGNPs are listed in Table S2 (Supporting Information). After the reaction, the samples rapidly cooled to room temperature.

Temperature Measurement: The temperature measurement was performed using an IR thermometer (Micro-Epsilon) with a temperature range of 200–1500 °C. The thermometer was connected to LabView

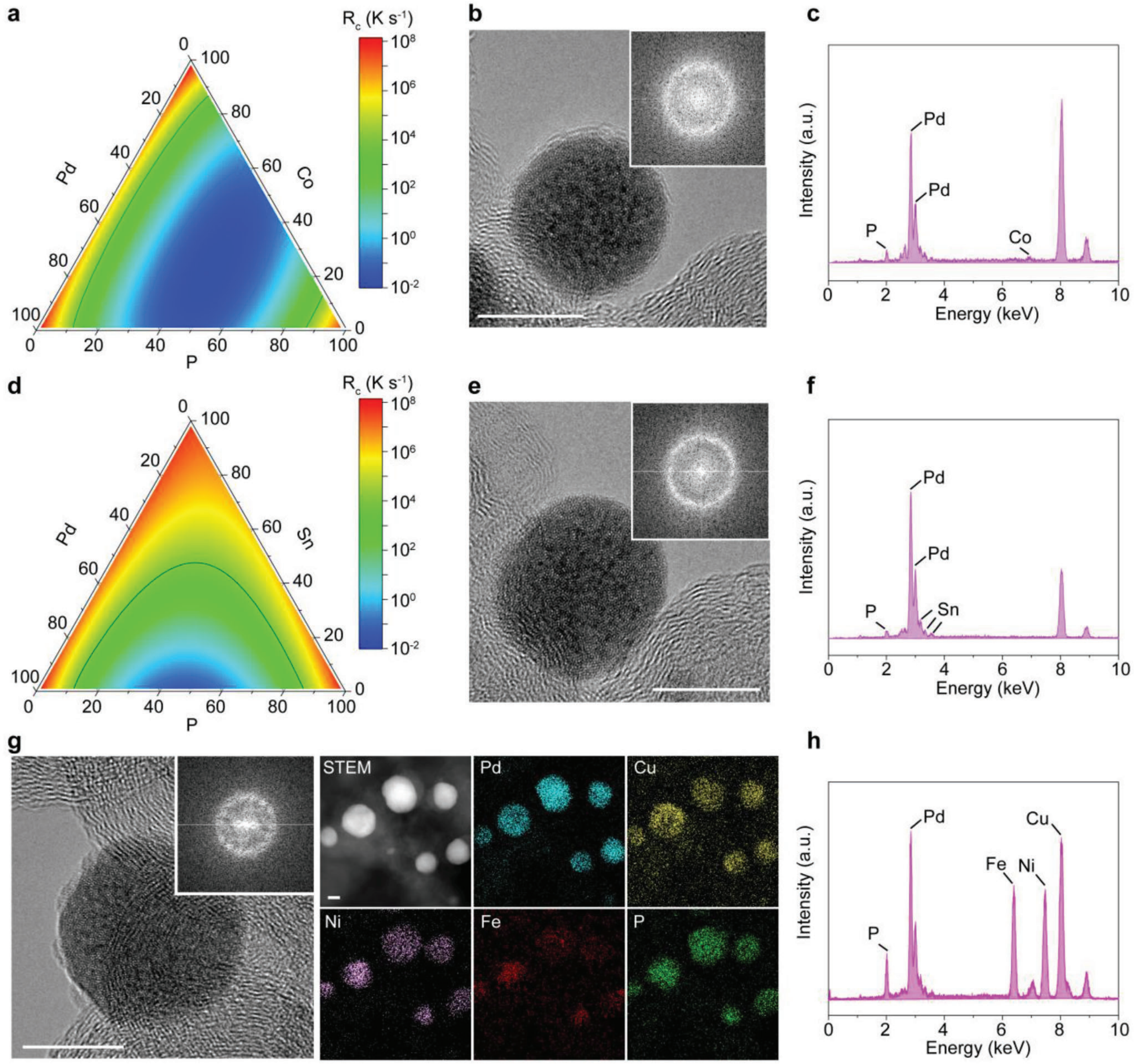

Figure 5. Nanoscale effect enhanced glass forming ability. a) Calculated R_C of the ternary Pd—Co—P system. The black line denotes $R_C = 10^4$ K s^{-1}. b) HRTEM image of PdCoP MGNP. Inset, the corresponding FFT pattern. c) EDS spectrum of PdCoP MGNP. d) Calculated R_C of the ternary Pd—Sn—P system. The black line denotes $R_C = 10^4$ K s^{-1}. e) HRTEM image of PdSnP MGNP. Inset, the corresponding FFT pattern. f) EDS spectrum of PdSnP MGNP. g) HRTEM image, the corresponding FFT pattern, HAADF-STEM image, and EDS maps of PdCuFeNiP MGNP. h) EDS spectrum of PdCuFeNiP MGNP. Scale bars, 10 nm.

through a Multifunction I/O (NI USB-6009) for real-time temperature recording with time resolution of 0.1 ms. Before use, the temperature was calibrated.

Characterization: Scanning electron microscopy (SEM) images were obtained using a FEI Quanta 400 ESEM Field Emission Microscope at 5 kV. EDS spectra were collected using the same system equipped with an EDS detector at 30 kV. XPS spectra were acquired on a PHI Quantera XPS system under a pressure of 5×10^{-9} Torr. Full XPS spectra were acquired with a step size of 0.5 eV and a pass energy of 140 eV, and elemental XPS spectra were acquired with a step size of 0.1 eV and a pass energy of 26 eV. XPS of P was collected after Ar$^+$ sputtering for 5 min to remove the surface layer of ≈5 nm to avoid surface oxidation when exposed in air. All XPS spectra were calibrated using the standard C 1s peak at 284.8 eV. XRD was conducted on a Rigaku SmartLab XRD using Cu Kα radiation (λ = 1.5406 Å). BF-TEM, HRTEM, and tilt-angle HRTEM images were collected using a JEOL 2100 field emission gun transmission electron microscope operating at 200 kV. SAED and nanobeam diffraction were collected using the same JEOL 2100F TEM system, and the diffraction patterns were calibrated using the Al standard. HAADF-STEM imaging and EDS mapping were carried out on a FEI Titan Themis3 system equipped with image and probe aberration corrections and an electron monochromator operating at 80 kV.

Ab Initio Molecular Dynamics (MD) Simulation of Atomic Structures of PdNiP MG: The density functional theory (DFT) method[43] implemented in the Vienna ab initio simulation package[44] was used. A plane wave expansion up to 500 eV was employed in combination with an all-electron-like projector augmented wave potential.[45] Exchange correlation was treated within the generalized gradient approximation using the functional parameterized by Perdew and Wang.[46] Both bulk MGs and their nanoparticle counterparts with the same composition were studied using the same method, potentials, and criteria of convergence for electronic band and atomic forces. The initial coordinates of atoms were generated using a random number generator with the constraint that all the atoms were closely packed in a box for bulk or a sphere for nanoparticle based on their bond lengths. Bulk MG was modeled in a supercell containing 420 atoms with the size of the supercell optimized. Nanoparticle MG was modeled in a sphere containing 313 atoms surrounded by a 10–15 Å thick vacuum layer. Since all the supercells were large enough, only Γ point was used for the Brillouin zone integration over a Monkhorst–Pack type mesh.[47] For structure optimization, the atoms were considered fully relaxed when the maximum force on each atom was smaller than 0.01 eV $\mathrm{Å}^{-1}$. The optimized structures were then annealed at ≈1500 K in a MD simulation, followed by rapid cooling to 300 K at a rate of 125 K ps^{-1}. The MD simulations were performed using Nose–Hoover thermostat and number–volume–temperature ensemble. The resulting atomic structures were then optimized, as shown in Figure S29 (Supporting Information).

Local Bond Orientational Order (BOO) Parameters: Local BOO parameters (Q_4 and Q_6) were calculated from the atomic models of both MG bulks and MG nanoparticles obtained by MD simulation, using the method described previously.[5,39] The distribution of the local BOO parameter for all the atoms in bulks and particles are shown in Figure 4e,f and Figure S30 (Supporting Information). A normalized BOO parameter was defined as $\sqrt{Q_4^2+Q_6^2}/\sqrt{Q_{4,\mathrm{fcc}}^2+Q_{6,\mathrm{fcc}}^2}$, where $Q_{4,\mathrm{fcc}}$ and the $Q_{6,\mathrm{fcc}}$ are the Q_4 and Q_6 parameters for perfect fcc structures.[5] This normalized parameter was between 0 and 1, where a larger value represented a more ordered structure. A normalized parameter value of 0.5 was used as the cutoff to separate the amorphous and ordered structures. The fraction of disordered atoms in the metallic glass was calculated (Figure S30k, Supporting Information).

Short-Range Order Analysis Based on Voronoi Tessellation and the Coordination Number: The Voronoi analysis of each atomic model of metallic glass was conducted by following a recent report.[5] The regulation was applied to each Voronoi polyhedron that those surfaces with areas less than 1% of the total polyhedron surface area were removed to minimize the degeneracy problem and thermal vibration effects.[40a] Each polyhedron was assigned an Voronoi index, $<n_3, n_4, n_5, n_6, \ldots>$, where n_i represented the number of i-edged faces of the polyhedron. After obtaining the Voronoi index, the coordination number of the center atom was calculated from $\sum_i n_i$.

Supporting Information

Supporting Information is available from the Wiley Online Library or from the author.

Acknowledgements

The authors thank Dr. Bo Chen of the Rice University for helpful discussion on XPS results, and Dr. Wenhua Guo of the Rice University for assistance in the electron diffraction. The funding of the research was provided by the Air Force Office of Scientific Research (Grant No. FA9550-22-1-0526), and the US Army Corps of Engineers, Engineer Research and Devlopment Center (ERDC) (Grant No. W912HZ-21-2-0050). The authors acknowledge the use of the Electron Microscopy Center (EMC) at the Rice University. The characterization equipment used in this project was, in part, from the Shared Equipment Authority (SEA) at the Rice University.

Conflict of Interest

A US provisional patent was filed by the Rice University on the synthesis of MGNP, where B.D. and J.M.T. were listed as the inventors, which has not yet been licensed. The authors declare no other competing interests.

Author Contributions

B.D. and Z.W. contributed equally to this work. B.D. conceived the idea and designed the experiments. B.D. conducted the synthesis, and most of the characterizations with the help of A.L., Y.C., S.X., and Q.L. Z.W., C.H.C., B.S., and Y.H. conducted the STEM and EDS mapping. D.X.L. and L.E. designed and built the setup. B.I.Y. and Y.Z. conducted the MD and DFT simulations. B.D. analyzed the simulation results with the assistance of Z.Y. G.L. conducted the heterogeneous catalysis test. B.D., Y.Z., and J.M.T. wrote and edited the paper. All aspects of the research were overseen by J.M.T. All authors discussed the results and commented on the paper.

Data Availability Statement

The data that support the findings of this study are available in the Supporting Information of this article.

Keywords

composition space, flash carbothermic reaction, high entropy, metallic glass, nanoparticles

Received: September 25, 2023
Revised: January 29, 2024
Published online:

---

[1] A. L. Greer, *Mater. Today* **2009**, *12*, 14.
[2] W. Klement, R. H. Willens, P. Duwez, *Nature* **1960**, *187*, 869.
[3] a) M. X. Li, S. F. Zhao, Z. Lu, A. Hirata, P. Wen, H. Y. Bai, M. W. Chen, J. Schroers, Y. H. Liu, W. H. Wang, *Nature* **2019**, *569*, 99; b) S. Y. Ding, Y. H. Liu, Y. L. Li, Z. Liu, S. Sohn, F. J. Walker, J. Schroers, *Nat. Mater.* **2014**, *13*, 494.
[4] a) H. W. Kui, A. L. Greer, D. Turnbull, *Appl. Phys. Lett.* **1984**, *45*, 615; b) M. Chen, *NPG Asia Mater.* **2011**, *3*, 82.
[5] Y. Yang, J. Zhou, F. Zhu, Y. Yuan, D. J. Chang, D. S. Kim, M. Pham, A. Rana, X. Tian, Y. Yao, S. J. Osher, A. K. Schmid, L. Hu, P. Ercius, J. Miao, *Nature* **2021**, *592*, 60.
[6] a) M. T. Kiani, C. M. Barr, S. C. Xu, D. Doan, Z. X. Wang, A. Parakh, K. Hattar, X. W. Gu, *Nano Lett.* **2020**, *20*, 6481; b) Z. D. Sha, Y. Teng, L. H. Poh, Q. X. Pei, G. C. Xing, H. J. Gao, *Acta Mater.* **2019**, *169*, 147; c) D. Jang, J. R. Greer, *Nat. Mater.* **2010**, *9*, 215.
[7] Y. Y. Shen, Y. Q. Li, C. Chen, H. L. Tsai, *Mater. Des.* **2017**, *117*, 213.
[8] G. Kumar, H. X. Tang, J. Schroers, *Nature* **2009**, *457*, 868.
[9] a) M. W. Glasscott, A. D. Pendergast, S. Goines, A. R. Bishop, A. T. Hoang, C. Renault, J. E. Dick, *Nat. Commun.* **2019**, *10*, 2650; b) J. Y. Li, G. Doubek, L. McMillon-Brown, A. D. Taylor, *Adv. Mater.* **2019**, *31*, 1802120; c) Y. C. Hu, Y. Z. Wang, R. Su, C. R. Cao, F. Li, C. W. Sun, Y. Yang, P. F. Guan, D. W. Ding, Z. L. Wang, W. H. Wang, *Adv. Mater.* **2016**, *28*, 10293; d) M. Carmo, R. C. Sekol, S. Y. Ding, G. Kumar, J. Schroers, A. D. Taylor, *ACS Nano* **2011**, *5*, 2979; e) F.-Y. Gao, S.-N. Liu, J.-C. Ge, X.-L. Zhang, L. Zhu, Y.-R. Zheng, Y. Duan, S. Qin, W. Dong, X. Yu, R.-C. Bao, P.-P. Yang, Z.-Z. Niu, Z.-G. Ding, W. Liu, S. Lan, M.-R. Gao, Y. Yan, S.-H. Yu, *Nat. Catal.* **2022**, *5*, 993; f) Y. Pang, S. Zhu, Z. Cui, Y. Liang, Z. Li, S. Wu, *Prog. Nat. Sci.: Mater. Int.* **2021**, *31*, 201.

[10] G. Kumar, A. Desai, J. Schroers, *Adv. Mater.* **2011**, *23*, 461.

[11] W. Yan, I. Richard, G. Kurtuldu, N. D. James, G. Schiavone, J. W. Squair, T. Nguyen-Dang, T. D. Gupta, Y. P. Qu, J. D. Cao, R. Ignatans, S. P. Lacour, V. Tileli, G. Courtine, J. F. Loffler, F. Sorin, *Nat. Nanotechnol.* **2020**, *15*, 875.

[12] T. Wada, D. V. Louzguine-Luzgin, A. Inoue, *Scr. Mater.* **2007**, *57*, 901.

[13] S.-X. Liang, S. Salamon, S. Zerebecki, L.-C. Zhang, Z. Jia, H. Wende, S. Reichenberger, S. Barcikowski, *Scr. Mater.* **2021**, *203*, 114094.

[14] a) Y. Ma, H. Wang, W. Lv, S. Ji, B. G. Pollet, S. Li, R. Wang, *RSC Adv.* **2015**, *5*, 68655; b) M. Zhao, K. Abe, S. Yamaura, Y. Yamamoto, N. Asao, *Chem. Mater.* **2014**, *26*, 1056; c) W. Wang, T. He, X. Yang, Y. Liu, C. Wang, J. Li, A. Xiao, K. Zhang, X. Shi, M. Jin, *Nano Lett.* **2021**, *21*, 3458.

[15] M. A. Zeeshan, D. Esque-de los Ojos, P. Castro-Hartmann, M. Guerrero, J. Nogues, S. Surinach, M. D. Baro, B. J. Nelson, S. Pane, E. Pellicer, J. Sort, *Nanoscale* **2016**, *8*, 1344.

[16] Y. H. Liu, J. B. Liu, S. Sohn, Y. L. Li, J. J. Cha, J. Schroers, *Nat. Commun.* **2015**, *6*, 7043.

[17] a) Y. Chen, G. C. Egan, J. Wan, S. Zhu, R. J. Jacob, W. Zhou, J. Dai, Y. Wang, V. A. Danner, Y. Yao, K. Fu, Y. Wang, W. Bao, T. Li, M. R. Zachariah, L. Hu, *Nat. Commun.* **2016**, *7*, 12332; b) S. Liu, Y. Shen, Y. Zhang, B. Cui, S. Xi, J. Zhang, L. Xu, S. Zhu, Y. Chen, Y. Deng, W. Hu, *Adv. Mater.* **2022**, *34*, 2106973; c) B. Deng, D. X. Luong, Z. Wang, C. Kittrell, E. A. McHugh, J. M. Tour, *Nat. Commun.* **2021**, *12*, 5794.

[18] a) Y. Yao, Z. Huang, P. Xie, S. D. Lacey, R. J. Jacob, H. Xie, F. Chen, A. Nie, T. Pu, M. Rehwoldt, D. Yu, M. R. Zachariah, C. Wang, R. Shahbazian-Yassar, J. Li, L. Hu, *Science* **2018**, *359*, 1489; b) Y. Yao, Z. Liu, P. Xie, Z. Huang, T. Li, D. Morris, Z. Finfrock, J. Zhou, M. Jiao, J. Gao, Y. Mao, J. Miao, P. Zhang, R. Shahbazian-Yassar, C. Wang, G. Wang, L. Hu, *Sci. Adv.* **2020**, *6*, eaaz0510; c) M. Cui, C. Yang, S. Hwang, M. Yang, S. Overa, Q. Dong, Y. Yao, A. H. Brozena, D. A. Cullen, M. Chi, T. F. Blum, D. Morris, Z. Finfrock, X. Wang, P. Zhang, V. G. Goncharov, X. Guo, J. Luo, Y. Mo, F. Jiao, L. Hu, *Sci. Adv.* **2022**, *8*, eabm4322; d) Y. Yao, Q. Dong, A. Brozena, J. Luo, J. Miao, M. Chi, C. Wang, I. G. Kevrekidis, Z. J. Ren, J. Greeley, G. Wang, A. Anapolsky, L. Hu, *Science* **2022**, *376*, eabn3103.

[19] B. Wang, C. Wang, X. Yu, Y. Cao, L. Gao, C. Wu, Y. Yao, Z. Lin, Z. Zou, *Nat. Synth.* **2022**, *1*, 138.

[20] a) W. Chen, Z. Wang, K. V. Bets, D. X. Luong, M. Ren, M. G. Stanford, E. A. McHugh, W. A. Algozeeb, H. Guo, G. Gao, B. Deng, J. Chen, J. T. Li, W. T. Carsten, B. I. Yakobson, J. M. Tour, *ACS Nano* **2021**, *15*, 1282; b) B. Deng, Z. Wang, W. Chen, J. T. Li, D. X. Luong, R. A. Carter, G. Gao, B. I. Yakobson, Y. Zhao, J. M. Tour, *Nat. Commun.* **2022**, *13*, 262; c) B. Deng, P. A. Advincula, D. X. Luong, J. Zhou, B. Zhang, Z. Wang, E. A. McHugh, J. Chen, R. A. Carter, C. Kittrell, J. Lou, Y. Zhao, B. I. Yakobson, Y. Zhao, J. M. Tour, *Nat. Commun.* **2022**, *13*, 5027.

[21] W. L. Johnson, G. Kaltenboeck, M. D. Demetriou, J. P. Schramm, X. Liu, K. Samwer, C. P. Kim, D. C. Hofmann, *Science* **2011**, *332*, 828.

[22] A. Takeuchi, A. Inoue, *Mater. Sci. Eng., A* **2001**, *304–306*, 446.

[23] A. T. D. Butland, R. J. Maddison, *J. Nucl. Mater.* **1973**, *49*, 45.

[24] a) H. S. Chen, *Mater. Sci. Eng.* **1976**, *23*, 151; b) H. S. Chen, *J. Non-Cryst. Solids* **1973**, *12*, 333.

[25] Y. He, R. B. Schwarz, *MRS Online Proc. Libr.* **1996**, *455*, 495.

[26] S. Lan, Y. Ren, X. Y. Wei, B. Wang, E. P. Gilbert, T. Shibayama, S. Watanabe, M. Ohnuma, X. L. Wang, *Nat. Commun.* **2017**, *8*, 14679.

[27] S. Kohiki, T. Hamada, *J. Mater. Sci.* **1990**, *25*, 1344.

[28] F. U. Hillebrecht, J. C. Fuggle, *Phys. Rev. B* **1982**, *25*, 3550.

[29] V. I. Nefedov, Y. V. Salyn, B. Walther, B. Messbauer, R. Schops, *Inorg. Chim. Acta* **1980**, *45*, L103.

[30] K. S. Kim, A. F. Gossmann, N. Winograd, *Anal. Chem.* **1974**, *46*, 197.

[31] Z. L. Jin, Y. P. Zhang, *Catal. Surv. Asia* **2020**, *24*, 59.

[32] Y. A. Wang, H. F. Liu, *J. Mol. Catal.* **1988**, *45*, 127.

[33] P. Bordeenithikasem, J. Liu, S. A. Kube, Y. Li, T. Ma, B. E. Scanley, C. C. Broadbridge, J. J. Vlassak, J. P. Singer, J. Schroers, *Sci. Rep.* **2017**, *7*, 7155.

[34] R. B. Schwarz, Y. He, in *Properties of Complex Inorganic Solids* (Eds: A. Gonis, A. Meike, P. E. A. Turchi), Springer US, Boston, MA **1997**.

[35] a) A. Takeuchi, N. Chen, T. Wada, Y. Yokoyama, H. Kato, A. Inoue, J. W. Yeh, *Intermetallics* **2011**, *19*, 1546; b) Y. J. Duan, L. T. Zhang, T. Wada, H. Kato, E. Pineda, D. Crespo, J. M. Pelletier, J. C. Qiao, *J. Mater. Sci. Technol.* **2022**, *107*, 82.

[36] G. Schluckebier, B. Predel, *Z. Metallkd.* **1983**, *74*, 569.

[37] A. Takeuchi, A. Inoue, *Mater. Sci. Eng., A* **2001**, *304*, 446.

[38] M. Gabski, M. Peterlechner, G. Wilde, *Entropy* **2020**, *22*, 292.

[39] W. Lechner, C. Dellago, *J. Chem. Phys.* **2008**, *129*, 114707.

[40] a) H. W. Sheng, W. K. Luo, F. M. Alamgir, J. M. Bai, E. Ma, *Nature* **2006**, *439*, 419; b) P. F. Guan, T. Fujita, A. Hirata, Y. H. Liu, M. W. Chen, *Phys. Rev. Lett.* **2012**, *108*, 175501.

[41] Y.-G. Yan, D. Lu, K. Wang, *Tungsten* **2023**, *5*, 32.

[42] a) R. K. Rai, K. Gupta, S. Behrens, J. Li, Q. Xu, S. K. Singh, *ChemCatChem* **2015**, *7*, 1806; b) G. Bao, J. Bai, C. Li, *Org. Chem. Front.* **2019**, *6*, 352.

[43] S. L. Dudarev, G. A. Botton, S. Y. Savrasov, C. J. Humphreys, A. P. Sutton, *Phys. Rev. B* **1998**, *57*, 1505.

[44] G. Kresse, J. Furthmuller, *Phys. Rev. B* **1996**, *54*, 11169.

[45] P. E. Blochl, *Phys. Rev. B* **1994**, *50*, 17953.

[46] J. P. Perdew, Y. Wang, *Phys. Rev. B* **1992**, *45*, 13244.

[47] H. J. Monkhorst, J. D. Pack, *Phys. Rev. B* **1976**, *13*, 5188.